MRS Advances © 2018 Materials Research Society
DOI: 10.1557/adv.2018.111

The Effect of Grain Boundaries and Second-Phase Particles on Hydride Precipitation in Zirconium Alloys

Said El Chamaa[1], Mitesh Patel[2], Catrin M. Davies[3] and Mark R. Wenman[1]

[1]*Department of Materials and Centre for Nuclear Engineering, Imperial College London, SW7 2AZ*

[2]*Department of Physics, Imperial College London, SW7 2AZ, UK*

[3]*Department of Mechanical Engineering, Imperial College London, SW7 2AZ, UK*

ABSTRACT

Understanding the precipitation of brittle hydride phases is crucial in establishing a failure criterion for various zirconium alloy nuclear fuel cladding. Accordingly, it is important to quantify the sensitivity of hydride precipitation to the component microstructure. This experimental investigation focuses on two microstructural characteristics and their role as hydride nucleation sites: The grain size and the alloy chemical composition. Samples of commercially pure zirconium (Zr-702) and Zircaloy-4, each with a wide range of grain sizes, were hydrided to 100 ppm and micrographs of the hydride distribution were optically analyzed for inter-granular and intra-granular precipitate sites. For most grain sizes, it was found that a significantly lower fraction of the precipitated hydrides nucleated at grain boundaries in Zircaloy-4 than in Zr-702, suggesting that a higher SPP content encourages the formation of intra-granular hydrides. Moreover, this effect became more prominent as the grain size increased; large-grain specimens contained a higher fraction of intra-granular hydrides than small-grain specimens of both Zr-702 and Zircaloy-4, highlighting the potency of grain boundaries as nucleation sites and how SPPs can influence the hydride distribution profile.

INTRODUCTION

Zirconium alloy cladding is central to the structural integrity of nuclear fuel pins as well as dry storage of spent fuel rods. However, zirconium (Zr) is susceptible to hydrogen pick-up in the reactor environment and, as a hydride-forming metal, its operation lifetime can be severely compromised by a hydrogen embrittlement mechanism known as delayed hydride cracking (DHC). The phenomenon of DHC constitutes three main sub-processes: (i) the atomistic diffusion of hydrogen to loaded stress-raisers; (ii) the microscale precipitation and growth of brittle zirconium hydride phase features at preferred nucleation sites; and (iii) the continuum fracture in the hydrogen-enhanced and hydride-rich zones. The repetition and interplay of diffusion,

precipitation and fracture in the vicinity of cracks and notches can ultimately lead to component failure and, hence, safeguarding against DHC is imperative [1–4].

Typical industry standards involve the use of empirical handbook solutions to predict DHC initiation, in specific materials, as a function of macroscopic parameters, such as the elastic moduli and component geometry [1]. Although this approach is convenient, the absence of microstructural information provides a very conservative analysis, which, in turn, complicates its application to the wide variety of materials that have been manufactured to have different textures and alloy compositions. As shown in Figures 1(a) and (b), macroscopic hydrides features can be observed both at the inter-granular and intra-granular sites, suggesting that grain boundaries (GBs) and second-phase particles (SPPs) are energetically-favorable nucleation sites. Accordingly, to generate microstructural models of hydride distribution and hence DHC, it is necessary to quantify the respective roles of GBs and SPPs in hydride precipitation. Therefore, one aim of DHC research concerns, in part, the development of advanced multi-physics computational models that are capable of exploring statistically the space of DHC failure criteria, which would be a cost-effective alternative to the expensive test programs. As shown in Figure 1(c), one necessary step towards this ideal is the ability to efficiently simulate micrographs of hydride distributions in various zirconium alloy microstructures. Therefore, this experimental work aims to provide insight onto the necessary parameters pertaining GBs and SPPs that could be useful for such microscale modelling of hydride precipitation [5, 6].

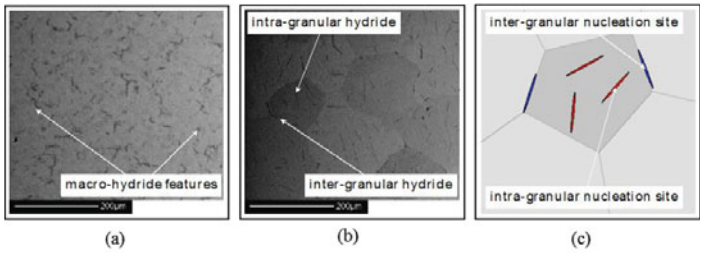

Figure 1. Secondary electron micrographs of hydrides in samples of Zircaloy-4 with (a) as-received small grains (~ 15 μm) and (b) heat treated large grains (~ 300 μm), which can be represented in (c) a computational framework that explicitly utilizes microstructural information.

This microscale investigation focuses on comparing the relative potency of GBs and SPPs as hydride nucleation sites. As a means of isolating the effects of SPPs, two sets of α-zirconium alloy samples were used, namely, the commercially-pure zirconium Zircadyne-702 (Zr-702) and a standard component material Zircaloy-4 (Zr-4), the latter of which has a higher SPP content than the former. For both sets of samples, specimens composed of various average grain sizes ℓ_G were used, ranging from the typical as-received metal microstructure ($\ell_G \simeq 10$ μm) to the problematic 'blocky-α' systems ($\ell_G \simeq 1000$ μm) [8]. The intermetallic SPP content was defined by the quantity of the typical low solubility alloying elements: iron (Fe) and chromium (Cr). Zr-702 contains maximum 0.20 wt. % of Fe+Cr, while Zr-4 contains 0.30– 0.37 wt. %. The specimens were then characterized using optical microscopy and scanning electron microscopy (SEM) imaging as well as electron backscatter diffraction (EBSD) analysis, which provided a direct comparison of intra-granular and inter-granular hydrides.

EXPERIMENTAL

Specimen Preparation

The specimens of Zr-702 and Zircaloy-4 were obtained by electro-discharge machining cuboids of dimensions 21.0 mm × 6.00 mm × 3.00 mm from hot-rolled recrystallized plates. For several specimens from both sets of samples, the average grain size was increased using a heat treatment technique proposed by Tong and Britton [8]. The heat treatment holds specimens at 800°C for 336 h (14 days) in an encapsulated argon atmosphere, followed by air cooling [8]. This treatment produced samples with ℓ_G between 300 – 600 μm as shown in Figure 2(b), as well as samples with so called blocky-α systems, possessing a bimodal grain distribution as shown in Figure 2(c). The SPP number density was quantified before and after this treatment using back-scattered SEM imaging (magnification factor of ~ 1000 – 2000). The SPP quantification proved that SPPs did not dissolve during the heat treatment, as the SPP number density was found to be the same before and after grain growth. The heat treatment may create a small fraction of β-Zr SPPs at GBs, but these nucleation sites are not distinguished from GBs in this study. Samples were electro-chemically hydrogen charged using a diluted sulphuric acid solution (2% H_2SO_4) at 65˚C followed by thermal diffusion at a hydride dissolution temperature of ~ 400˚C for 7 hours. Samples were then allowed to furnace cool for 24 hours to form stable δ-hydride features. The details of the hydrogen charging technique can be found in the work of Weekes et al. [10]. The inert gas fusion (IGF) technique was used to measure the hydrogen concentration, as outlined in the ASTM E1447 standard [7]. EBSD was used to determine the texture and grain size of the as-received plates and the thermally treated samples. EBSD samples were electro-polished using a mixture of 10% perchloric acid and 90% methanol at 25 Volts and a temperature of ~ −42˚C [10]. Finally, image analysis software *Image-J* was used to convert optical, SEM and EBSD micrographs into a binary format after background subtraction using a grayscale threshold limit. Upon processing the binary micrographs, shown in Figure 2(d, e, f), the total number density of hydrides was determined, as a function of the grain size, for the two materials. This hydride number density was further distinguished into percentages of intra-granular and inter-granular hydrides; the ratio η of intra-to-inter granular hydrides provides a simple strategy of comparing the relative potency of GBs and SPPs.

Results

Figure 2(a) shows a secondary electron micrograph of as-received Zr-702, revealing an equiaxed, homogenous α-Zr grain structure containing a hydrogen concentration of 100 ± 18.4 ppm. The average number density of macro-hydride precipitation was quantified to be 374 ± 70.5 and 103 ± 17.5 hydrides mm^{-2} for Zircaloy-4 small (15 ± 2.8 μm) and large grains ($600 - 900$ μm), respectively. This was marginally lower for Zr-702 where the average hydride number density was calculated to be 246 ± 60.7 and 99 ± 11.34 hydrides mm^{-2} for small ℓ_G (50 ± 6.9 μm) and large ℓ_G (200 – 900 μm), respectively. Figure 3(a) shows that around 45% of hydrides precipitated within the small grains of the Zircaloy-4 samples compared to 12% for the small grained Zr-702 samples. Considering the difference in grain size and the hydride density between these alloys was small, this is attributed to the difference in SPP content, which is higher in Zircaloy-4 at 0.0345 ± 0.0230 SPPs μm^{-2} compared to 0.0186 ± 0.0199 SPPs μm^{-2} in Zr-702, leading to more intra-granular precipitation and showing that SPPs do actively change hydride nucleation. As ℓ_G was increased from 15 – 50 μm to 200 – 900 μm, for both alloys, the percentage of hydrides that precipitated within grains increased in both Zircaloy-4 (from 45% to 82%) and in Zr-702 (from 12% to 74%)

highlighting the potency of the grain boundaries as hydride nucleation sites. However, again in Zircaloy-4, with the higher SPP density, intra-granular precipitation was still higher at 82% compared to 74% in Zr-702 again presumably because of the role of SPPs acting as intra-granular sites in the Zircaloy-4 alloy.

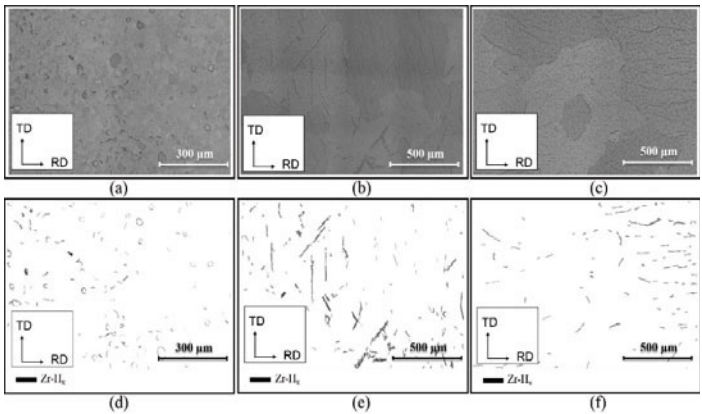

Figure 2. (a) Secondary electron micrographs of Zr-702 in the RD – TD section (average grain size ~ 50 μm). Uniform grain size enhancement, in Zr-702, to ~ 300 μm is shown in (b) and bimodal grain size distribution is shown in (c) containing the so called blocky-α systems. Binary images of the micrographs are respectively shown in (d), (e) and (f) revealing the dark macro-hydride features.

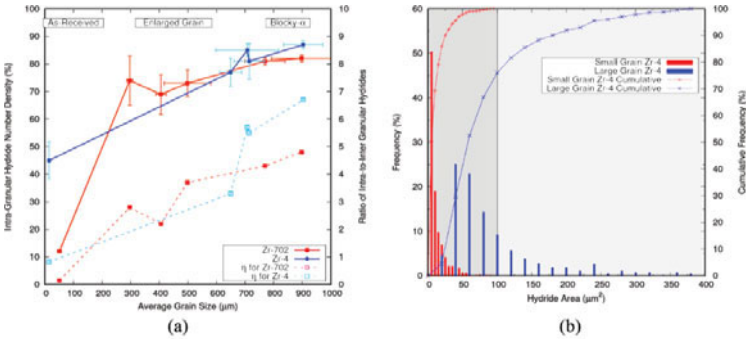

Figure 3. Hydride profile distributions parameterized by grain size and SPP content, as represented by (a) the proportion of intra-granular and inter-granular hydrides for Zr-702 and Zircaloy-4 specimens of differing average grain sizes, and (b) the macro-hydride area distribution in Zircaloy-4 for an as-received sample with $\ell_G \simeq 15$ μm and an enhanced grain size sample with $\ell_G \simeq 715$ μm. Horizontal and vertical error bars show the standard deviation of the average grain size and the proportion of intra-granular and inter-granular hydrides, respectively.

The hydride size distribution in Zircaloy-4, characterized by the area of each macro-hydride packet is shown in Figure 3(b). In the small grained sample around 50% of hydrides were found to have an area between 5.0 – 9.0 μm^2 ranging up to 90 μm^2 ($<$ 1%). This area distribution was found to be significantly different in samples with ℓ_G of 715 ± 53.4 μm, where ~ 50% of hydrides were found to have areas between 40 – 79 μm^2 and ranging up to 380 μm^2($<$ 1%).

DISCUSSION

It is evident that GBs are highly potent nucleation sites in both the presence and absence of SPPs in the commercially pure Zr-702 and Zircaloy-4, respectively. Referring to Figure 3(a), this can be seen for the small-grain Zr-702 samples, which can contain significantly higher proportions of inter-granular hydrides than their larger grain counterparts. As zirconium hydrides are distinct thermodynamic phases defined by their stoichiometric and crystallographic properties, this may fundamentally be attributed to the hierarchy of heterogeneous nucleation sites in metals. Generally, nucleation sites are stress-raisers with favorable defect structures that provide desirable conditions for precipitation; in this formalism, GBs are presumed to be the most favorable [1, 13]. Therefore, small-grain samples have a high fraction of inter-granular hydrides as they contain a high density of GBs. The formation of hydrides at GBs is also linked to the slow cooling rate following the hydrogen homogenization treatment, which allows hydrogen diffusion to remain fast for a longer period of time before hydrogen is trapped at nucleation sites at the point of the precipitation temperature. This ensures that the hydride distribution pattern has sufficient time to attain the most optimal free energy configuration, which is reflected in the activation of the GB nucleation sites that are most energetically favorable.

It is also worthwhile to note that GBs control the morphological growth of inter-granular hydride features, as shown in Figure 2. Again, this can be traced fundamentally to the geometry of GBs as planar defects, whose local compatibility mismatch stresses are most pronounced along the length of the interface between highly-misorientated adjacent crystallites. Therefore, given the potency of GBs, the texture will have a significant effect on both the nucleation and growth of hydrides. Moreover, it appears that GBs also affect the size of the hydrides, considering Figure 3(b). Here, the hydride size corresponds to the area of a macroscopic hydride feature that is, upon closer inspection, a composite stack structure of microscopic pure hydride phase platelets [1, 12]. In the smaller grain samples, the high density of GBs can disrupt the regularity of the micro-hydride stacking, leading to the formation of smaller macro-hydrides [9, 11]. These results indicate the importance of GBs as nucleation sites; therefore, computational models of hydride precipitation should aim to incorporate GBs explicitly.

In contrast to GBs, the role of SPPs in influencing hydride precipitation is best seen by considering the enhanced grain and blocky-α specimens from both sample sets. As seen in Figure 3(a), there are more intra-granular hydrides in large-grain samples. From the standpoint of stress analysis, the interface between the intermetallic inclusions and the parent matrix may be thought of as a more localized variant of a GB-like defect. Accordingly, the effect of SPPs as nucleation sites is analogous to GBs; however, as SPPs are generally less potent stress-raisers than GBs, the role of SPPs as nucleation sites only becomes more influential as the density of GBs decreases. Again, this agrees with the theory of heterogeneous nucleation for phase transformations in metals. As shown in Figure 3(a), this effect was more prominent for Zircaloy-4 (higher SPP content) as opposed to Zr-702 as expected. Therefore, in computational models of hydride precipitation, materials should ideally be distinguished by SPP content; for example, this can be achieved by invoking microstructural parameters that quantify the density of intra-granular nucleation sites that represent the random population of SPPs within grains.

In summary, the experimental results in Figure 2 and Figure 3 provide a valuable insight into the parameter space associated with GBs and SPPs as two important classes of nucleation sites. In particular, it is essential that models of hydride precipitation should include the microstructural information that characterizes the texture and alloy composition through inter- and intra-granular nucleation sites. Such

information can be implemented by explicitly treating GBs and SPPs, which can be respectively represented by a Voronoi tessellation of convex polygons and geometrical objects specified by point-in-polygon algorithms. This would be a simple backdrop to existing multi-field diffusion-precipitation solvers that would appropriately capture the effects of GBs and SPPs.

CONCLUSIONS

Hydride precipitation in zirconium was quantified for materials with different grain sizes and alloy compositions to compare GBs and SPPs as nucleation sites. It was found that for smaller grain specimens, there was a higher proportion of inter-granular hydrides, relative to intra-granular hydrides, due to the higher GB density. But, as the grain sizes were enhanced, the proportion of intra-granular hydrides increased; this effect was more prominent for specimens with a higher SPP content. These results can be used to parametrize microstructural models of hydride precipitation that are able to explore more fully the space of GB and SPP nucleation.

ACKNOWLEDGMENTS

This research is supported by the EPSRC under the grants EP/L015900/1 and EP/G036888/1 as well as an industrial collaboration with Rolls-Royce plc.

REFERENCES

1. M.P. Puls, The Effect of Hydrogen and Hydrides on the Integrity of Zirconium Alloy Components: Delayed Hydride Cracking, 1st ed. (Springer, London, 2012) p. 7–336.
2. D. Northwood, Mater. Des. **6** (2) 58–56 (1985).
3. J. Gros and J. Wadier, J. Nucl. Mater. **172** (1) 85–96 (1990).
4. Kearns, J. Nucl. Mater. **22** (3) 292–303 (1967).
5. M. Patel, S. Waheed, M.R. Wenman, A.P. Sutton and D.S. Balint, MRS Advances **2** (55) 3353–3358 (2017).
6. S. Shi, G. Shek and M.P. Puls, J. Nucl. Mater. **218** (2) 189–201 (1995).
7. ASTM International in *Standard Test Method for Determination of Hydrogen in Titanium and Titanium Alloys by Inert Gas Fusion Thermal Conductivity/Infrared Detection Method* (ASTM E1447, 2009).
8. V. Tong and T. Britton. Acta Mater. **129** 510–520 (2017).
9. L. Bramwell, J. Haste, D. Worswick and D. Parsons in *An Experimental Investigation into the Oxidation of Zircaloy-4 at Elevated Pressures in the 750 to 1000ºC Temperature Range* (Zirconium in the Nuclear Industry: Tenth International Symposium, ASTM STP 1245, 1994).
10. H. Weekes, N. Jones, T. Lindley and D. Dye, J. Nucl. Mater. **478** 32–41 (2016).
11. D. Westlake, J. Nucl. Mater. **16** 215–219 (1965).
12. C. Ells, J. Nucl. Mater. **28** (2) 129–151 (1968).
13. J.W. Christian, The Theory of Transformations in Metals and Alloys, 3rd ed. (Pergamon, Amsterdam, 2002) p. 356.